Applied Surface Science 520 (2020) 146369

Contents lists available at ScienceDirect

Applied Surface Science

journal homepage: www.elsevier.com/locate/apsusc

Suppressing the luminescence of V_{cation}-related point-defect in AlGaN grown by MOCVD on HVPE-AlN

Ke Jiang[a,b], Xiaojuan Sun[a,b,*], Jianwei Ben[a,b,c], Zhiming Shi[a,b], Yuping Jia[a,b], Yang Chen[a,b], Shanli Zhang[a,b], Tong Wu[a,b], Wei Lü[a,d], Dabing Li[a,b,*]

[a] State Key Laboratory of Luminescence and Applications, Changchun Institute of Optics, Fine Mechanics and Physics, Chinese Academy of Sciences, Changchun 130033, China
[b] Center of Materials Science and Optoelectronics Engineering, University of Chinese Academy of Sciences, Beijing 100049, China
[c] College of Materials Science and Engineering, Shenzhen University, Shenzhen 518071, China[1]
[d] Key Laboratory of Advanced Structural Materials, Ministry of Education, Changchun University of Technology, Changchun 130012, China

ARTICLE INFO

Keywords:
AlGaN
Point-defect
Metallization pretreatment
Luminescence
Carrier recombination

ABSTRACT

AlGaN materials have a great prospect in ultraviolet and deep-ultraviolet optoelectronic devices, while the point-defects impede their applications. In this report, we successfully suppressed the luminescence of V_{cation}-related point-defect in AlGaN materials. AlGaN epilayers were grown on AlN/sapphire template by metal-organic chemical vapor deposition and the mixed metal-organic flows were used to pretreat the surface of AlN/sapphire template. The luminescence intensity of $(V_{cation}\text{-complex})^{2-}$ point-defects was reduced by the pretreatment, demonstrating the favorable suppression effect on the luminescence of $(V_{cation}\text{-complex})^{2-}$ point-defects. The ephemeral metal-rich condition and metal-droplets on the AlN/sapphire template were believed to be partially responsible for the suppression. It also supported the conception that the 3.90 eV luminescence in AlN originated from the V_{cation}-related point-defects rather than the C_N point-defects. The surface morphology was investigated and an optimized pretreating time of 60 s was obtained. The carrier recombination mechanism was also studied and the results revealed that dislocations not only could act as non-radiative recombination centers, but also could bind the excitons.

1. Introduction

Ultraviolet (UV) and deep-ultraviolet (DUV) optoelectronic devices are broadly utilized in the applications of sterilization and disinfection, coating curing, lithograph, secret communication, quantum teleportation and so on [1–3]. However, with the banning of the mercury lamps, UV and DUV light sources become increasingly scarce and people are trying to search for the high efficient, energy saving and portable alternatives. AlGaN materials have attracted extensive attention due to the direct and tunable wide-bandgap from 3.4 to 6.2 eV [4]. Actually, some AlGaN-based optoelectronic devices such as UVC light-emitting diodes (UVC-LEDs), laser diodes (LDs) and photodetectors (PDs) had ever been realized in recent years [5–7]. However, the performances of those devices are far from real applications. On the one hand, the internal quantum efficiency is low due to the high dislocation density in the AlGaN epilayers [8].On the other hand, the doping efficiency is low and the device lifetime is short, which are both partially due to the high point-defect density in the AlGaN epilayers [9,10].

Nowadays, many approaches have been proposed to improve the AlGaN crystal quality. The so-called two-steps method [11], three-steps method [12], low-temperature (LT) or middle-temperature (MT) interlayer method [13], epitaxial lateral overgrowth (ELOG) method [14], and high-temperature (HT) thermal annealing method [15] are all applied to promote the quality of AlN/sapphire templates and thus the subsequent AlGaN epilayers. It is possible to obtain AlGaN epilayers with dislocation density as low as 10^8 cm^{-2}. Moreover, the commercialization of 2 in. single-crystal AlN substrates and thick hydride vapor phase epitaxy grown AlN/sapphire (HVPE-AlN/sapphire) templates with high DUV transmittance and mirror-like surface provided another effective way to further elevate the performances of the AlGaN-based devices [16,17]. Despite of the considerable reduction of dislocation density in AlGaN, the device lifetime and reliability cannot be

* Corresponding authors at: State Key Laboratory of Luminescence and Applications, Changchun Institute of Optics, Fine Mechanics and Physics, Chinese Academy of Sciences, Changchun 130033, China.
E-mail addresses: sunxj@ciomp.ac.cn (X. Sun), lidb@ciomp.ac.cn (D. Li).
[1] Current affiliation.

https://doi.org/10.1016/j.apsusc.2020.146369
Received 24 January 2020; Received in revised form 28 March 2020; Accepted 6 April 2020
Available online 18 April 2020
0169-4332/

guaranteed, for which the point-defects should mainly be responsible.

There are longstanding investigations into the point-defects in III-nitrides. The famous yellow luminescence (YL) near 2.15 eV in GaN was widely observed, which was believed to be resulted from the V_{Ga} point-defects [18–20]. Otherwise, a deep level of about 0.18 eV below the conduction band was also observed, which was attributed to the V_N point-defects [21]. Those point-defects seriously deteriorated the GaN-based devices. As for AlN, analogous extrinsic light emissions were also observed. Low energy emissions located at 3.40, 3.90, and 4.71 eV appeared, and those emissions were respectively classified as the levels of point-defects V_{Al}^{3-}, $(V_{Al}\text{-complex})^{2-}$, and $(V_{Al}\text{-complex})^{1-}$ [22,23]. There were also controversies about the origins of the light emissions. Ramon Collazo et al. believed that the luminescence of 3.90 eV originated from the C_N point-defects [24]. On the other respect, an emission about 0.26 eV below the conduction band was observed, which was attributed to the V_N point-defects [25]. In AlGaN ternary alloys, the point-defects related light emissions were more universally discovered. They were also ascribed to the V_{cation}-related point-defects [22,23]. Despite of the extensive investigations on point-defects, there are no effective methods to reduce the point-defect density, which impedes the applications of AlGaN-based devices.

Theoretical calculations demonstrated that the formation energy of V_N in metal-rich conditions was lower than that in N-rich conditions while the formation energy of V_{cation} in metal-rich conditions was higher than that in N-rich conditions [26]. This result indicates that it is possible to suppress the formation of point-defects by controlling the growth conditions. In the metal-organic chemical vapor deposition (MOCVD) growth procedures, it is easy to achieve N-rich condition due to the comparatively high V/III ratio. The increase of hole concentration in p-AlGaN grown in high V/III ratio confirmed the conception due to the effective suppression to the V_N point-defects [27–29]. However, it is quite difficult to realize steadily metal-rich condition in MOCVD, indicating the difficulty to suppress the V_{cation}-related point-defects.

Previous studies had used the metal-organics flow to pretreat the substrate to improve the III-nitrides quality [30–32], which could provide ephemeral metal-rich conditions. In this report, a method of metallization pretreatment was applied to suppress the luminescence of V_{cation}-related point-defects in AlGaN epilayers grown on HVPE-AlN/sapphire template substrate by MOCVD. The luminescence of V_{cation}-related point-defect was suppressed due to the ephemeral metal-rich condition and metal-droplets on substrates and the optimized metallization pretreating time was 60 s. It also demonstrated that the 3.90 eV luminescence in AlN originated from V_{cation}-related point-defects rather than C_N point-defects.

2. Materials and methods

The AlGaN epilayers were grown on HVPE-AlN/sapphire templates with sapphire cutoff angle of 1.5 ± 0.2° toward the a-plane by AIX200/4 RF-S HT-MOCVD system. The thicknesses of HVPE-AlN were all about 5 μm. The trimethyl aluminum (TMAl), trimethyl gallium (TMGa), and ammonia (NH_3) were used as Al, Ga and N precursors, respectively, and the hydrogen (H_2) was used as the carrier gas. The chamber pressure and total flow rate were fixed at 40 mbar and 9600 sccm during the AlGaN growth. The flow rates of metal-organics TMAl and TMGa were 40 and 12 sccm, and the flow rate of NH_3 was 500 sccm. To pretreat the surface of HVPE-AlN, the TMAl and TMGa flows were kept open and the NH_3 was kept closed for 600, 60, and 20 s at the beginning of AlGaN growth, which are denoted as samples B, C, and D, respectively. For comparison, the AlGaN epilayers without metallization pretreatment were also grown, which is denoted as sample A. The growth time of all AlGaN epilayers was 40 min and the resulted AlGaN epilayers were all about 1.2 μm.

High angle annular dark field scanning (HAADF) transmission electron microscopy (STEM) was used to investigate the interface between HVPE-AlN substrate and the AlGaN epilayer. Energy Dispersive Spectroscopy (EDS) mapping was measured to determined the growth condition and the element profile. The D8 discover thin film X-ray diffractometer (XRD) was used to determine the Al content of all samples. The X-ray is Cu $K_{\alpha 1}$ radiation line with wavelength of 0.15406 nm. The Bruker Multimode 8 atomic force microscopy (AFM) was used to analyze the surface evolution. The photoluminescence (PL) spectra and time-resolved PL (TRPL) decay spectra were measured to analyze the optical and carrier recombination properties. PL spectra at RT were excited by a laser with wavelength and out-put power of 213 nm and 50 mW. Temperature-dependent PL and TRPL measurements were carried out by a femtosecond laser with wavelength and out-put power of 217 nm and 20 mW at temperature ranging from 10 to 300 K. The diameter of the laser spot is about 2 mm. The repetition frequency of the light pulse is 76 MHz. The laser beams horizontally illuminated on the vertically placed wafers and the geometry was adjusted to attain the highest PL intensity and lowest noise. Once the geometry was obtained, all wafers were measured in the same geometry. Five spots were recorded for each samples to eliminate the fortuity.

3. Results and discussions

Fig. 1(a) shows the HAADF-STEM image of sample C. Samples B and D exhibit the same interface characteristics as sample C. It can be seen that the pretreatment can form an interlayer between HVPE-AlN and AlGaN epilayer. The corresponding EDS mappings of the elements profile of Carbon, Aluminum, and Gallium are displayed in Fig. 1(b)–(d). At the interface areas (in the white rectangles), the Carbon and Aluminum concentrations are obviously higher than other areas, and the Gallium element is also sparingly observed, indicating the metal-organics decomposed during the pretreatment and constructed a metal- as well as carbon-rich growth condition.

Fig. 2(a) and (b) are the XRD 2theta-omega scanning results of the (0 0 0 2) and (1 0 –1 2) planes for samples A, B, C, and D, respectively. The peak positions of the (0 0 0 2) planes for the AlGaN epilayers in samples A to D are 35.282°, 35.235°, 35.345°, and 35.345°, respectively. These of the (1 0 –1 2) planes are 49.086°, 49.157°, 48.835°, and

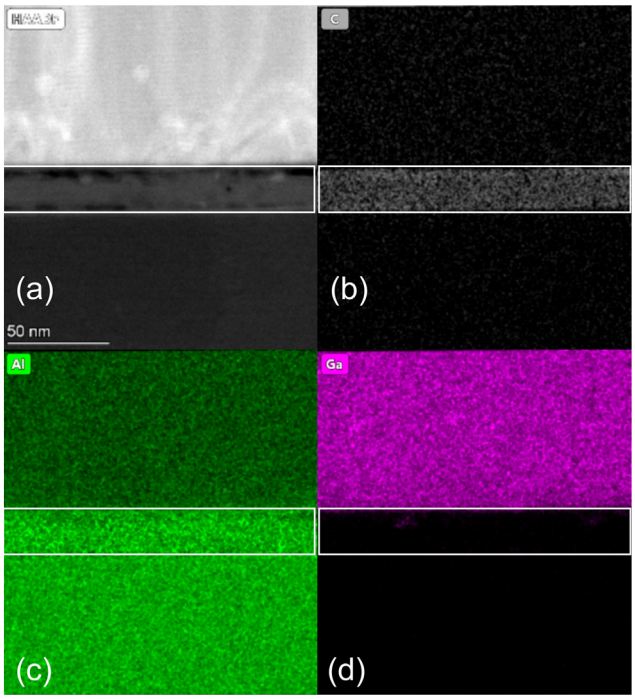

Fig. 1. The (a) HAADF-STEM image of sample C and the corresponding element profile of (b) Carbon, (c) Aluminum, and (d) Gallium, respectively.

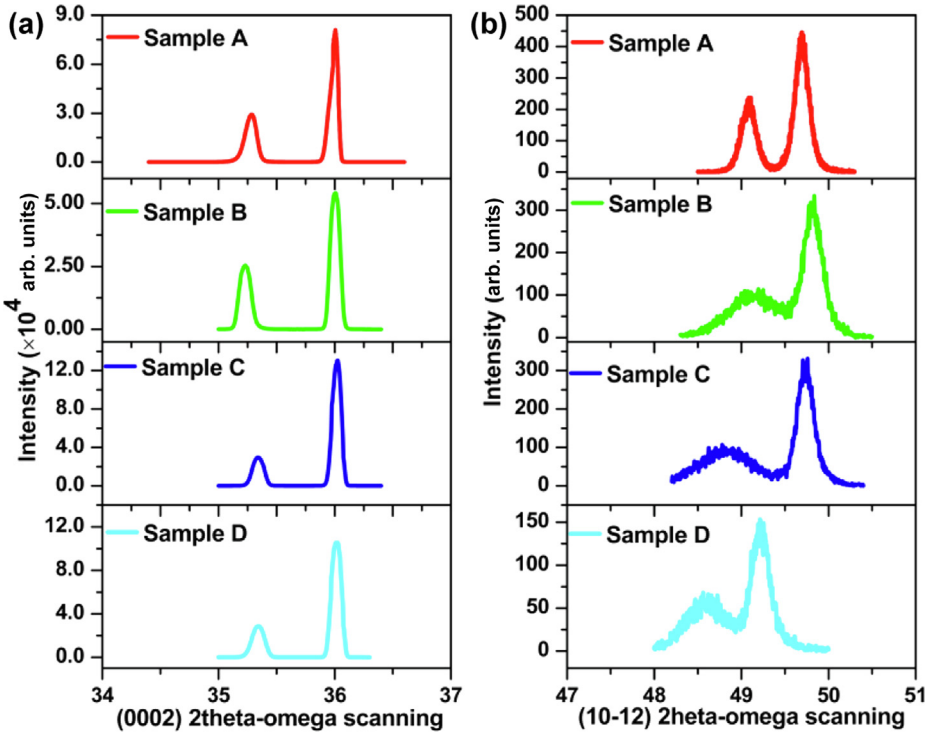

Fig. 2. The 2theta-omega scanning of (a) (0 0 0 2) planes and (b) (1 0 –1 2) planes of samples A, B, C and D, respectively.

48.610°, respectively. According to the Bragg's law and inter-planar space formula of hexagonal structures, the in-plane and out-plane lattice constants of ***a*** and ***c*** for the samples A to D can be determined as 0.31311, 0.31175, 0.31714, 0.32002 nm and 0.50836, 0.50902, 0.50748, 0.50748 nm, respectively. It is reasonable to assume the III-nitrides satisfy the biaxial-stress condition because of their hexagonal structures [33]. Based on the assumption, the Al content in the AlGaN epilayers can be calculated. During the calculations, the elastic constants C_{13}, C_{33}, C_{13}, and C_{33} of AlN and GaN were taken the values of 108, 373, 103, and 405 GPa, respectively [34]. The lattice constants ***a*** and ***c*** of free-strained AlN and GaN were taken the values of 0.31127, 0.31892, 0.49817, and 0.51850 nm, respectively [35,36]. The elastic constants of AlGaN were obtained by linear interpolation method and the lattice constants of free-strained AlGaN were obtained by Vegard's Low [37]. Eventually, the Al content in the AlGaN epilayer for sample A was determined as 59% and these for samples B to D were 49%, respectively. Additionally, it can be also deduced from the Full-Width-Half-Maximum of the XRD results that the dislocation density of sample A is lower than that of samples B to D (Supporting information).

The defect-related luminescence information was characterized by PL as Fig. 3. As it can be seen in Fig. 3(a), there are four obvious peaks labeled as P_A1, P_A2, P_A3 and P_A4 in sample A, respectively. The peak P_A1 located at 4.662 eV is the near-band-edge emission. Besides, previous studies have demonstrated that the peak P_A2 originated from the macro-step areas where the Al content was lower than the flat areas due to the bunching effect [38–40]. The peak P_A3 located at 4.232 eV is resulted from the deep donor level transition. Not surprisingly, a commonly observed PL peak in AlGaN also appeared in sample A as the peak P_A4 located at 3.062 eV. As for samples B to D, the results are similar to each others while are quite different from that of sample A. There are two obvious peaks located at 4.477 and 4.306 eV in samples B to D labeled as $P_{BCD}1$ and $P_{BCD}2$, which originate from near-band-edge emission and shallow donor level transition, respectively. However, there are no obvious peaks in samples B to D analogous to P_A4 in sample A. To more distinctly investigate the luminescence properties, log-scale spectra are plotted as the insertion in Fig. 3(a). Two additional peaks at 3.513 and 2.904 eV can be noticed, shown as $P_{BCD}3$ and $P_{BCD}4$. Although there were still defect-related luminescence in samples B to D, the intensities of the peaks drastically decreased compare to sample A.

As discussed above, the dislocation densities in samples B to D are higher than that in sample A, which can introduce non-radiative recombination centers. It is essential to investigate whether the defect-related luminescence suppression in samples B to D comes from the point-defect density reduction or the non-radiative recombination enhancement. Assuming that non-radiative recombination can be neglected at LT because the photo-generated non-equilibrium carriers can hardly transport to non-radiative recombination centers at very low temperature, the LT PL spectra can be utilized to determine the origin of the defect-related luminescence reduction. Fig. 3(b) shows the fitted PL spectra at 10 K for samples A and D (Supporting Information). The near-band-edge emission of the two samples exhibits similar intensity, indicating the non-radiative recombination are negligible as assumed above. While the defect-related luminescence of sample D is obviously lower than that of sampe A. This is a signal implying that the metallization pretreatment was effective to suppress the point-defect related luminescence and the suppression effect at least partially came from the reduction of the point-defect density. Otherwise, temperature-dependent PL spectra for samples A and D indicated non-radiative recombination also contributed to the point-defect related luminescence reduction, which will be discussed later. The normalized PL spectra as shown in Fig. 3(c) indicated that the pretreating time of 60 s exhibited better suppression effect than 600 and 20 s.

To determine the type of the point-defect, it is necessary to find out the origins of the peaks P_A4, $P_{BCD}3$ and $P_{BCD}4$. Fig. 3(d) displays the PL spectrum of the HVPE-AlN templates. An intense peak located at 3.513 eV labeled as $P_{HVPE\text{-}AlN}$ was observed, which was quite coincident to the positions of peak $P_{BCD}3$, indicating the peaks $P_{BCD}3$ resulted from the HVPE-AlN templates. Fig. 4(a) plots the PL peak energies from Ref. [22,23] as the function of Al content [22,23]. The peaks P_A1, $P_{BCD}1$, P_A4, $P_{BCD}4$ and $P_{HVPE\text{-}AlN}$ are also plotted in Fig. 4(a). It can be clearly seen that these dots almost align at four lines, indicating the emissions can be classified into four types. To further identify the defect types, the energy level positions of each peaks in the bandgap as the function of Al content need to be obtained. The equation

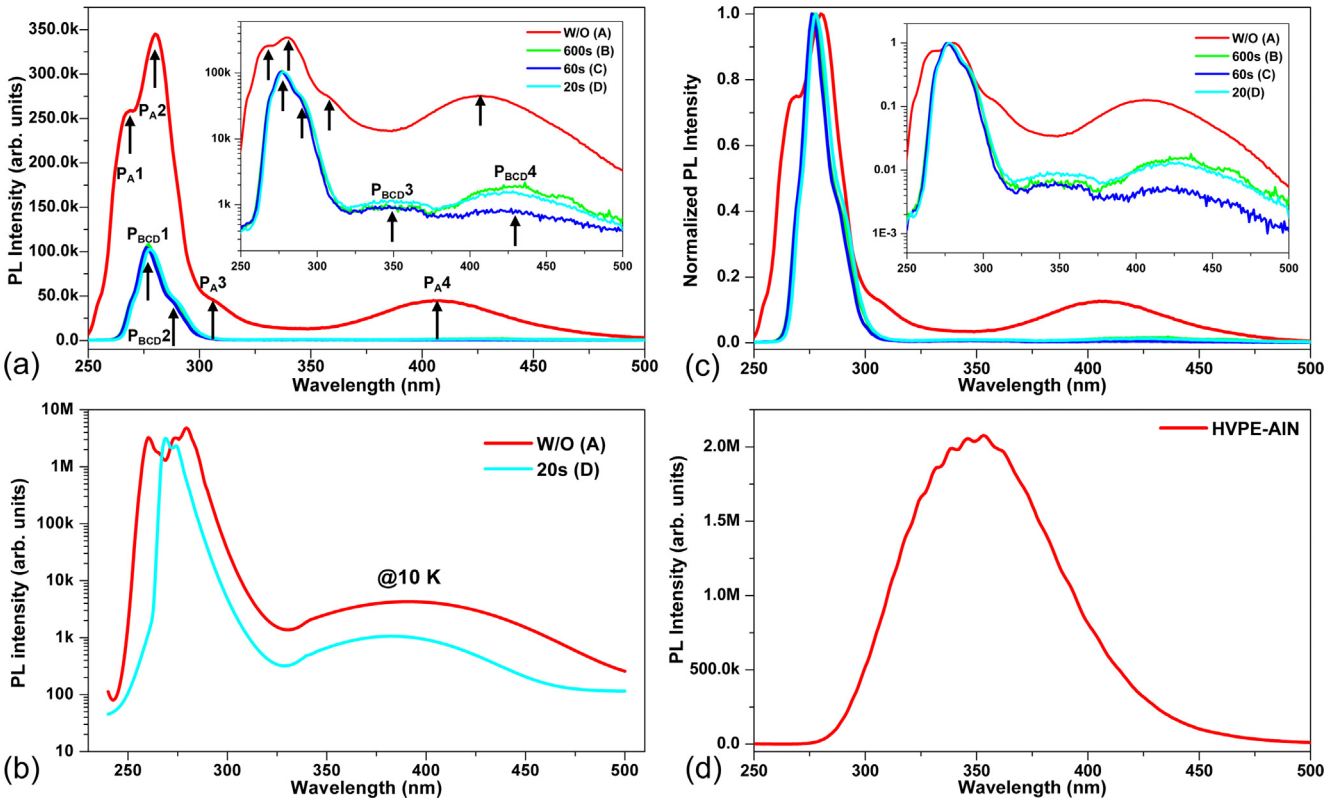

Fig. 3. (a) is the PL spectra of samples A, B, C and D at RT by laser with 213 nm wavelength, respectively. The insertion is the corresponding log-scale spectra. (b) is the fitted PL spectra of samples A and D at low temperature of 10 K by laser with 217 nm wavelength. (c) is the normalized PL spectra at RT. The insertion is the corresponding log-scale spectra. (d) is the PL spectrum of the HVPE-AlN template at RT by laser with 213 nm wavelength.

$$E_g = x{\cdot}E_g(AlN) + (1-x){\cdot}E_g(GaN) - b{\cdot}x{\cdot}(1-x) \quad (1)$$

was utilized to calculated the bandgap of AlGaN, where the AlN bandgap $E_g(AlN)$, GaN bandgap $E_g(GaN)$ and the bowling parameter b were taken as 6.2, 3.4, and 1 eV, respectively [4,41]. The conduction band offset $\Delta E_c(x)$ and valence band offset $\Delta E_v(x)$ between $Al_xGa_{1-x}N$ and GaN had been assumed to 70% and 30% of the bandgap offset ΔE_g

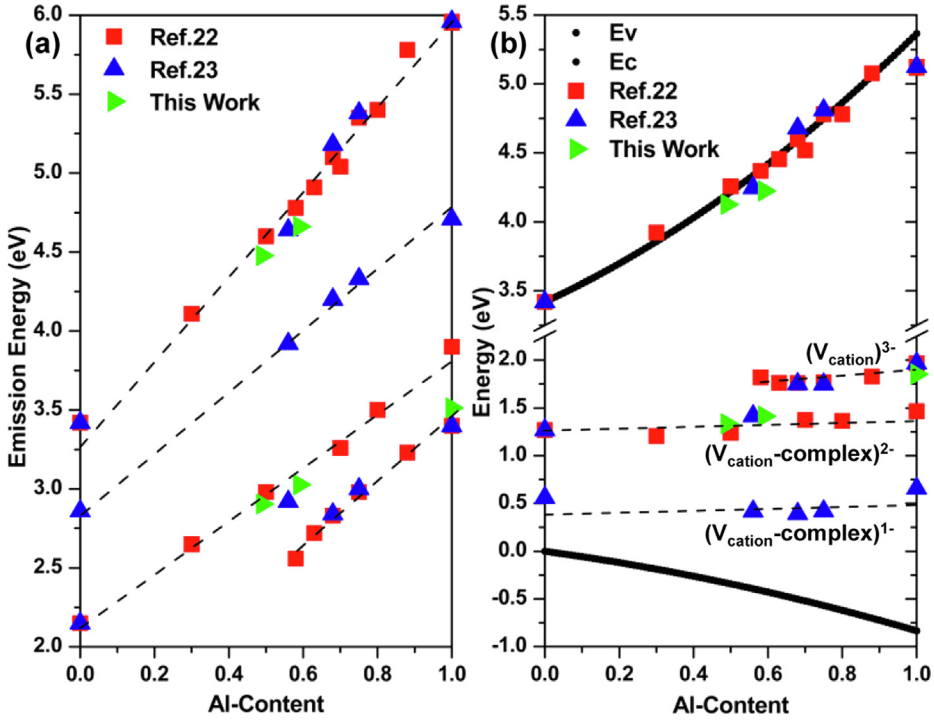

Fig. 4. (a) The PL peak energies from Refs. [22,23] and Fig. 3 as function of Al-content at RT, respectively. (b) Deep acceptor levels related to V_{cation}-related point-defects obtained from Refs. [22,23] and Fig. 3 as well as the E_c and E_v as function of Al-content at RT, respectively.

(x). Taking the valence band of GaN as the reference zero energy level, the conduction band $E_c(x)$ of $Al_xGa_{1-x}N$ can be calculated by

$$E_c(x) = E_c(GaN) + 0.7\cdot(E_g(x) - E_g(GaN)) \quad (2)$$

and the valence band $E_v(x)$ of $Al_xGa_{1-x}N$ can be calculated by

$$E_v(x) = -0.3\cdot(E_g(x) - E_g(GaN)) \quad (3)$$

The resulted E_c and E_v are plotted as the black dot curves in Fig. 4(b). The energy level positions of the near-band-edge emission $E_{NBE}(x)$, which aligned at the first line from top to bottom in Fig. 4(a), were determined by

$$E_{NBE}(x) = E_v(x) + E_{emission}(Al_xGa_{1-x}N) \quad (4)$$

where $E_{emission}(Al_xGa_{1-x}N)$ was the measured emission peak energy. Similarly, the energy level positions of the point-defects related emissions $E_A(x)$, which align at the second to fourth lines from top to bottom in Fig. 4(a), can be also determined by

$$E_A(x) = E_c(x) - E_{emission}(Al_xGa_{1-x}N) \quad (5)$$

Eventually, the energy levels' profile was displayed as Fig. 4(b).

As it can be seen in Fig. 4(b), the energy levels of high energy emission are all arranged close to E_c, confirming the P_A1 and $P_{BCD}1$ are resulted from near-band-edge emission. More importantly, it can be clearly seen that there are three levels pinning in the bandgap, namely the levels scarcely vary with Al content. Previous studies demonstrated that the three pinning levels were resulted from three different point-defects V_{cation}^{3-}, $(V_{cation}\text{-}complex)^{2-}$ and $(V_{cation}\text{-}complex)^{1-}$, respectively [22,23]. The level of $P_{HVPE\text{-}AlN}$ is located at the top level and those of P_A4 and $P_{BCD}4$ are exactly located at the middle level as the green dots in Fig. 4 (b). So it can be deduced that the luminescence P_A4, $P_{BCD}4$ in samples A to D originate from the $(V_{cation}\text{-}complex)^{2-}$ point-defects. Thus the metallization pretreatment can reduce the density of $(V_{cation}\text{-}complex)^{2-}$ point-defects. During the pretreatment, ephemeral metal-rich condition was formed and metal-droplets deposited on the surface. The metal-rich condition and metal-droplets should be responsible for the reduction of $(V_{cation}\text{-}complex)^{2-}$ point-defect. On the other hand, it is reasonable to categorize the origin of the 3.9 eV emission in AlN and the point-defect related emissions in this work into similar categories according to Fig. 4. If the 3.9 eV emission in AlN is resulted from C_N, it can also infer the point-defect related emissions in this work originated from C_N. However, the pretreatment not only can provide metal-rich condition, but also can create Carbon-rich condition [42,43], which can increase the C_N point-defect density and result in more intense defect-related emission. But it is just the opposite, which indicates the 3.90 eV luminescence in AlN originated from the V_{cation}-related point-defects rather than the C_N.

Besides the suppression effect on the formation of point-defects, the influences of the metallization pretreatment on the surface morphology of AlGaN epilayers were also investigated to optimize the pretreating time. Fig. 5(a)–(d) display the AFM images of samples A to D with scale of 10 μm × 10 μm, respectively. There are obvious macro-steps with wide steps and unstraight step edges in the surface of sample A as shown in Fig. 5 (a). It had been demonstrated that the macro-steps were resulted from the cutoff angle in sapphire of the HVPE-AlN templates [44]. After pretreatment, the width of the macro-steps remarkably became narrower as shown in Fig. 5(b)–(d). Moreover, the macro-step arrangement of sample C is better than that of samples B and D. Noticing the scale bar beside the images, it can be known that the flatness of sample C is also better than that of samples A, B and D, namely the pretreating time of 60 s is best among the four samples. Taking the point-defect suppression effect and surface morphology evolution into consideration, the pretreating time of 60 s is believed to be the most appropriate time, while further optimization is needed, comprehensively.

The temperature-dependent PL spectra were also measured to investigate the carrier recombination processes. Fig. 6 depicts the fitted PL spectra of samples A and D at temperature from 10 to 300 K (Supporting information). With temperature increasing, the PL peak position slightly shifts with a typical "*S*-shape", which originates from the alloy-potential fluctuation [40]. The sample A exhibits larger shift than sample D, implying sample A has stronger alloy fluctuation. On the other aspect, the PL intensity of both samples decreases with temperature increasing, indicating the presence of non-radiative recombination. The decrement of sample D is larger than that of sample A, demonstrating the non-radiative recombination in sample D is stronger than that in sample A. This is mainly resulted from the higher dislocation density in sample D. For the point-defect related luminescence, it decreases with increasing temperature as well. Such decrease demonstrates the non-radiative recombination centers can also influence the point-defect luminescence. So it can be deduced that both the reduction of the point-defect density and the non-radiative recombination centers caused the suppression of point-defect luminescence. Note that the point-defect luminescence cannot be detected at temperature > 210 K for sample A and > 120 K for sample D, for which we believe the lower output power of the femtosecond laser and the quartz window of low temperature chamber are responsible.

The carrier recombination mechanism was also studied by TRPL spectra. Fig. 7(a) and (b) shows the normalized TRPL of the near-band-edge emissions P_A1 and $P_{BCD}1$ of samples A and D at temperature from 10 to 300 K, respectively. To extract the effective PL decay lifetimes, a single exponential law as the equation

$$I(t) = I_0\cdot exp(t/\tau_{PL}) \quad (6)$$

was used to fit the TRPL spectra, where $I(t)$ is the PL intensity at time t, I_0 is the initial PL intensity, and τ_{PL} is the effective PL decay lifetime. Otherwise, a biexponential law that

$$I(t) = I_1\cdot exp(t/\tau_1) + I_2\cdot exp(t/\tau_2) \quad (7)$$

was applied to fit the decay spectra if the single exponential law did not work well, where I_i is the initial intensity of ith component and τ_i reflects the lifetime of the corresponding radiative recombination processes [45,46]. The effective PL lifetime is obtained through the formula

$$\tau_{PL} = (I_1\cdot\tau_1^2 + I_2\cdot\tau_2^2)/(I_1\cdot\tau_1 + I_2\cdot\tau_2) \quad (8)$$

when the biexponential low is applied. A multi-exponential law can also be used to fit the TRPL decay spectra. The more terms the fitting law contains, the more extrinsic radiative recombination processes there are. The fast decay constant potentially reflect the intrinsic radiative recombination process [45,46]. For sample A, the single exponential law can fit the TRPL spectra from 10 to 120 K, while only biexponential law can function at temperature > 120 K. From the RTPL and temperature-dependent PL spectra as Figs. 3 and 6, Al-content non-uniform level and deep donor level existed, causing the P_A2 and P_A3 emissions, respectively. With temperature increasing, transports among these levels took effects, resulting in the transition from single exponential law to biexponential law. For sample D, a biexponential law was needed to fit the TRPL spectra, indicating there always other radiative recombination channel. The shallow donor level, whose emission is always distinct at temperature from 10 to 300 K as shown in Fig. 6, might be the other radiative recombination channel.

The extracted effective PL lifetimes of samples A and D are plotted in Fig. 7(c) and (d). The radiative and non-radiative recombination lifetimes were calculated by

$$1/\tau_{PL}(T) = 1/\tau_r(T) + 1/\tau_{nr}(T) \quad (9)$$

$$\tau_r(T) = \tau_{nr}(T)/IQE(T) \quad (10)$$

$$IQE(T) = \int PL(T)/\int PL(10\ \mathrm{K}) \quad (11)$$

where $\tau_{PL}(T)$,$\tau_r(T)$,$\tau_{nr}(T)$, $IQE(T)$, and $\int PL(T)$ are the effective PL decay lifetime, radiative recombination lifetime, non-radiative recombination lifetime, internal quantum efficiency, and integrated PL intensity at

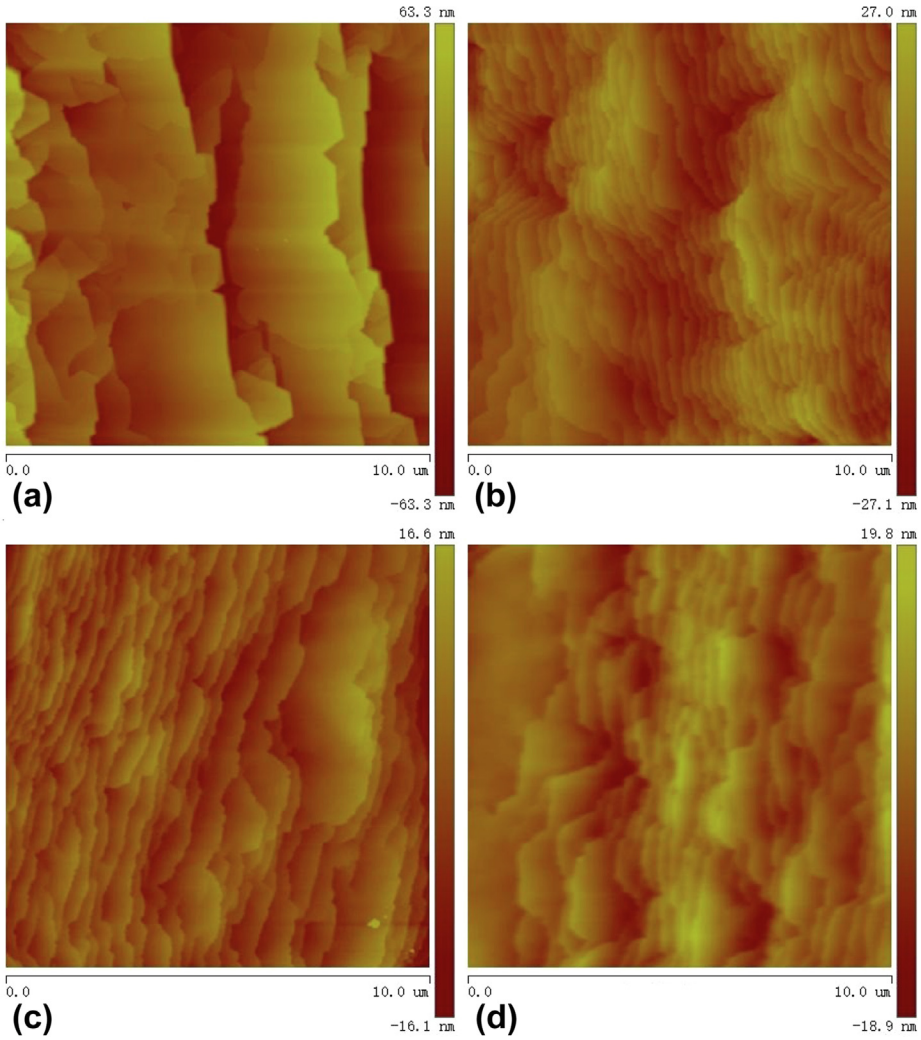

Fig. 5. (a), (b), (c), (d) are the AFM images of samples A, B, C, D with scale of 10 μm × 10 μm, respectively.

temperature of T (K). The internal quantum efficiency at 10 K was assumed to be 100%. The resulted $\tau_r(T)$, and $\tau_{nr}(T)$ are also plotted in Fig. 7(c) and (d). Previous theoretical studies had demonstrated the temperature-dependent radiative recombination lifetime could reflect the exciton dimensionality characteristics. The radiative recombination lifetime of zero-dimensional (0D) exciton is independent of T, while those of two-dimensional (2D) and three-dimensional (3D) excitons are proportional to T and $T^{1.5}$, respectively [47,48]. For sample A, the radiative recombination lifetime exponentially increases with increasing temperature at the entire temperature range, exhibiting 3D exciton behavior. For sample D, different phenomena were observed. At temperature < 40 K, the radiative recombination lifetime linearly increases with temperature increasing, exhibiting 2D exciton behavior. At medium temperature from 40 to 150 K, the radiative recombination lifetime scarcely alter with temperature increasing, exhibiting 0D exciton behavior. At higher temperature from 150 to 300 K, the radiative recombination lifetime exponentially increases with temperature increasing, exhibiting 3D exciton behavior.

Comparing the exciton dimensionality of sample A to D, it was found the excitons in sample D exhibited lower dimensionality than that in sample A at temperatures < 150 K, indicating the excitons in sample D suffered stronger binding effect than that in sample A. Our previous work revealed that the alloy potential fluctuation of sample D was lower than that of sample A [40]. So it can be speculated the excitons in sample D might not mainly be confined by alloy potential fluctuation. There are another bound centers in sample D. Generally, the enhancement of binding effect can prevent excitons from diffusing to non-radiative recombination centers, thus promoting the quantum efficiency. However, the quantum efficiency of sample D is lower than that of sample A. This phenomenon indicated that the bound centers might directly act as the non-radiative recombination centers. Defects including point-defects and dislocations are usually the non-radiative recombination centers. However, based on the decrease of the point-defect density and increase of the dislocation density in sample D compared to sample A, it can be deduced that dislocations might be the bound centers as well as non-radiative recombination centers.

Based on the discussions, it was found the metallization pretreatment to the surface of the HVPE-AlN template substrate can suppress the luminescence of the $(V_{cation}\text{-}complex)^{2-}$ point-defect. The suppression resulted from the reduction of the point-defect density, on the one respect, and also resulted from the non-radiative recombination centers, on the other respect. The dislocations usually act as the non-radiative centers. Moreover, the dislocations can also act as the exciton bonding centers. It is quite harmful for improving the quantum efficiency of near-band-edge emission. Hence, the method needs to be further optimized to reduce not only the point-defect density, but also the dislocation density. Upon the method of metallization pretreatment, we can provide an optimization direction that to periodically metalize the epilayer surface and grow the AlGaN layer. By adjusting the metallization pretreating time and the AlGaN layer thickness within one period and the total circles, it is hopeful to realize AlGaN epilayers with reduced concentration of the V_{cation}-related point-defect as well as the

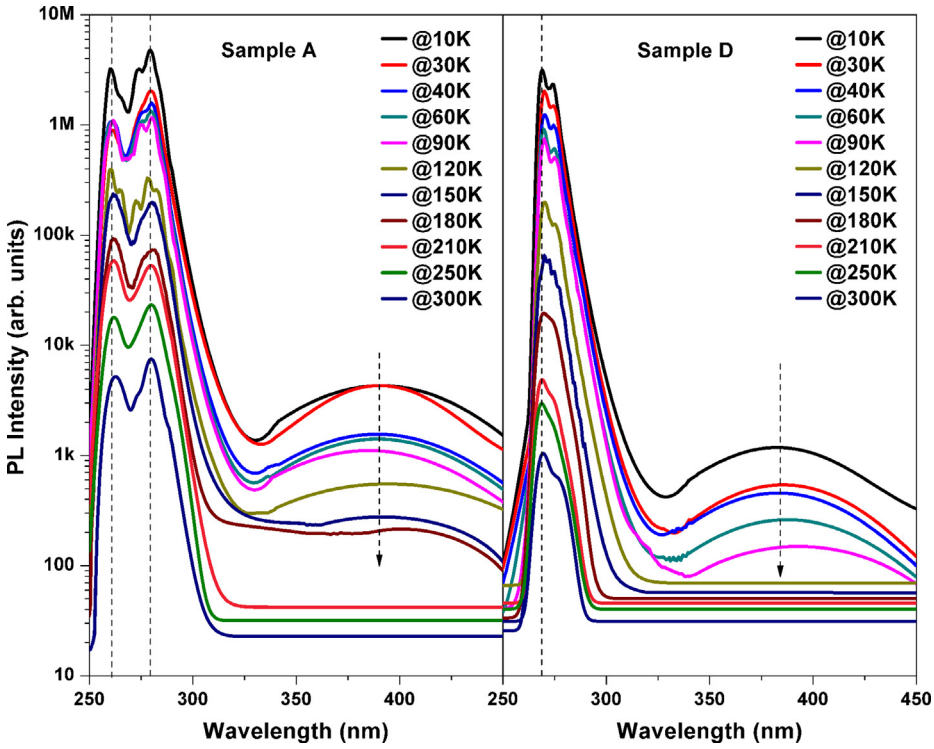

Fig. 6. The fitted PL spectra excited by the femtosecond laser at temperature from 10 to 300 K of samples A and D.

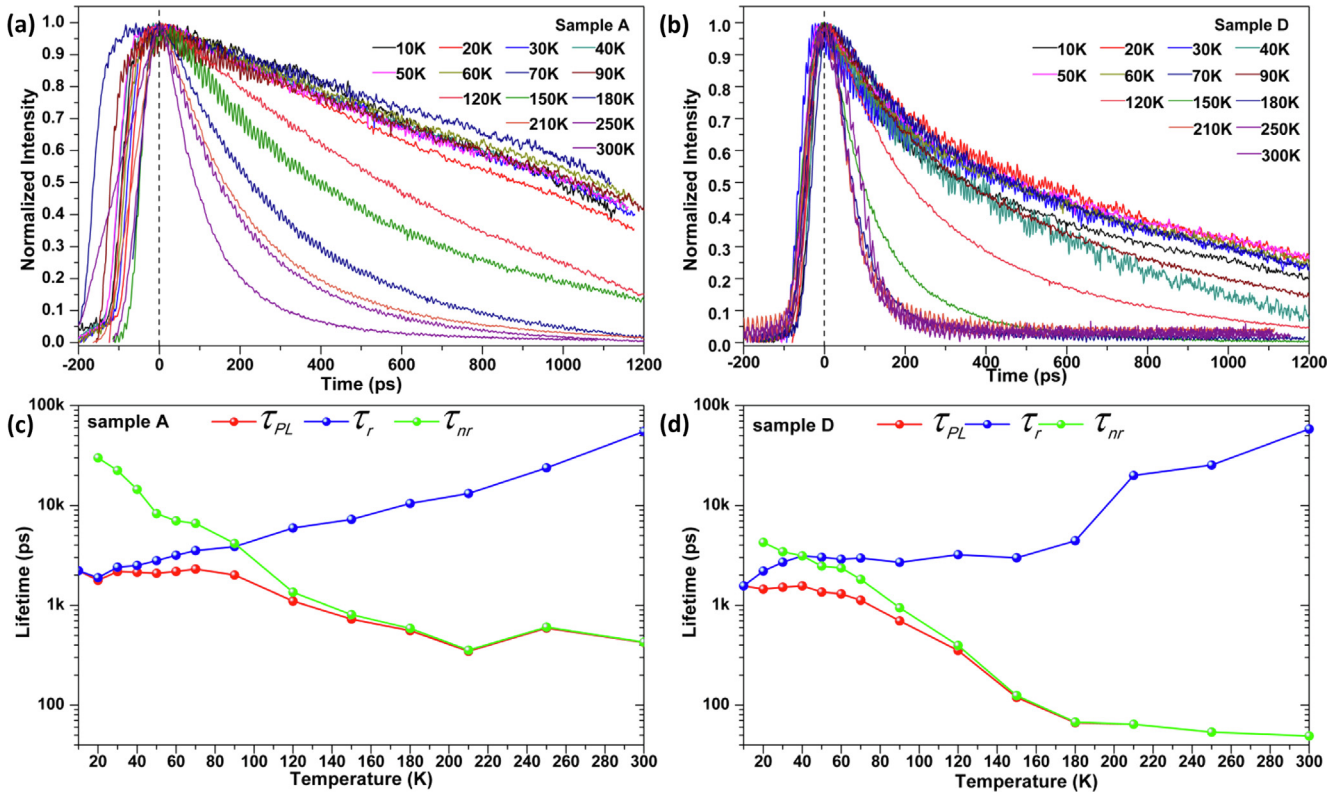

Fig. 7. (a) and (b) are the normalized TRPL decay spectra for samples A and D, respectively. (c) and (d) are the effective PL lifetimes, radiative and non-radiative recombination lifetimes for samples A and D, respectively.

dislocation non-radiative recombination centers.

4. Conclusions

In summary, a method of metallization pretreatment to the surface of the HVPE-AlN template substrate has been proposed to suppress the luminescence of point-defects. With the mixed metal-organic flows (TMAl and TMGa) pretreating, the luminescence of $(V_{cation}\text{-}complex)^{2-}$ point-defects decreased. The ephemeral metal-rich condition and metal-droplets on the HVPE-AlN were believed to be partially responsible for the suppression. It also supported the conception that the 3.90 eV luminescence in AlN originated from V_{cation}-related point-defects rather than C_N point-defects. Taking the surface morphology into consideration, an optimized pretreating time of 60 s was obtained. Furthermore, it was found the metallization pretreatment could alter the exciton dimensionality characteristics, which demonstrated that dislocations not only could act as non-radiative recombination centers, but also could bind the excitons. Further optimization needs to be performed to reduce not only the point-defect density, but also the dislocation density.

CRediT authorship contribution statement

Ke Jiang: Conceptualization, Methodology, Formal analysis, Investigation, Writing - original draft, Writing - review & editing, Visualization. **Xiaojuan Sun:** Conceptualization, Methodology, Formal analysis, Investigation, Supervision, Project administration, Funding acquisition. **Jianwei Ben:** Methodology, Formal analysis. **Zhiming Shi:** Methodology, Formal analysis. **Yuping Jia:** Methodology, Formal analysis. **Yang Chen:** Methodology, Formal analysis. **Shanli Zhang:** Methodology, Formal analysis. **Tong Wu:** Methodology, Formal analysis. **Wei Lü:** Methodology, Formal analysis. **Dabing Li:** Conceptualization, Methodology, Formal analysis, Investigation, Supervision, Project administration, Funding acquisition.

Declaration of Competing Interest

The authors declare that they have no known competing financial interests or personal relationships that could have appeared to influence the work reported in this paper.

Acknowledgments

This work was supported by the National Key R&D Program of China [2016YFB0400101], National Science Fund for Distinguished Young Scholars [61725403], National Natural Science Foundation of China [61574142, 61874118, 61827813, 11705206], Key Program of the International Partnership Program of CAS [181722KYSB20160015], Jilin Provincial Science & Technology Department [20180201026GX], Youth Innovation Promotion Association of CAS [Y201653, Y201945].

Appendix A. Supplementary material

Supplementary data to this article can be found online at https://doi.org/10.1016/j.apsusc.2020.146369.

References

[1] Y. Pulin, Y. Naichia, L. Chin-Hai, D. Ting-Jou, Applications of LEDs in optical sensors and chemical sensing device for detection of biochemicals, heavy metals, and environmental nutrients, Renew. Sustain. Energy Rev. 75 (2017) 461–468, https://doi.org/10.1016/j.rser.2016.11.011.

[2] H.Y. Lin, C.W. Sher, D.H. Hsieh, X.Y. Chen, H.M.P. Chen, T.M. Chen, K.M. Lau, C.H. Chen, C. Lin, H.C. Kuo, Optical crosstalk reduction in a quantum-dot-based full-color micro-light-emitting diodes display by a lithographic-fabricated photoresist mold, Photon. Res. 5 (2017) 411–416, https://doi.org/10.1364/PRJ.5.000411.

[3] K.R. Son, B.R. Lee, M.H. Jang, H.C. Park, Y.H. Cho, T.G. Kim, Enhanced light emission from AlGaN/GaN multiple quantum wells using the localized surface plasmon effect by aluminum nanoring patterns, Photon. Res. 6 (2018) 30–36, https://doi.org/10.1364/PRJ.6.000030.

[4] P. Rinke, M. Winkelnkemper, A. Qteish, D. Bimberg, J. Neugebauer, M. Scheffler, Consistent set of band parameters for the group-III nitrides AlN, GaN, and InN, Phys. Rev. B 77 (2008) 075202, https://doi.org/10.1103/PhysRevB.77.075202.

[5] D.Y. Kim, J.H. Park, J.W. Lee, S. Hwang, S.J. Oh, J. Kim, C. Sone, E.F. Schubert, J.K. Kim, Overcoming the fundamental light-extraction efficiency limitations of deep ultraviolet light-emitting diodes by utilizing transverse-magnetic-dominant emission, Light: Sci. Appl. 4 (2015) e263.

[6] Y. Harumasa, Y. Yoji, K. Masakazu, K. Hirofumi, Demonstration of an ultraviolet 336 nm AlGaN multiple-quantum-well laser diode, Appl. Phys. Lett. 93 (2008) 241106, https://doi.org/10.1063/1.3050539.

[7] D.B. Li, X.J. Sun, H. Song, Z.M. Li, Y.R. Chen, H. Jiang, G.Q. Miao, Realization of a high-performance GaN UV detector by nanoplasmonic enhancement, Adv. Mater. 24 (2012) 845–849, https://doi.org/10.1002/adma.201102585.

[8] K. Ban, J. Yamamoto, K. Takeda, K. Ide, M. Iwaya, T. Takeuchi, S. Kamiyama, I. Akasaki, Amano H, Internal quantum efficiency of whole composition-range AlGaN multiquantum wells, Appl. Phys Express 4 (2011) 052101, https://doi.org/10.1143/APEX.4.052101.

[9] D.B. Li, K. Jiang, X.J. Sun, C.L. Guo, AlGaN photonics: recent advances in materials and ultraviolet devices, Adv. in Opt. and Photon. 10 (2018) 43–110, https://doi.org/10.1364/AOP.10.000043.

[10] T. Mattila, R.M. Nieminen, Point-defect complexes and broadband luminescence in GaN and AlN, Phys. Rev. B 55 (1997) 9571–9576, https://doi.org/10.1103/PhysRevB.55.9571.

[11] X.J. Sun, D.B. Li, Y.R. Chen, H. Song, H. Jiang, Z.M. Li, G.Q. Miao, Z.W. Zhang, In situ observation of two-step growth of AlN on sapphire using high-temperature metal-organic chemical vapour deposition, CrystEngComm 15 (2013) 6066, https://doi.org/10.1039/C3CE40755A.

[12] M.L. Nakarmi, B. Cai, J.Y. Lin, H.X. Jiang, Three-step growth method for high quality AlN epilayers, Phys. Status Solidi A 209 (2012) 126–129, https://doi.org/10.1002/pssa.201127475.

[13] X.H. Li, S. Wang, H.G. Xie, Y.O. Wei, T.T. Kao, M.M. Satter, S.C. Shen, P.D. Yoder, T. Detchprohm, R.D. Dupuis, A.M. Fischer, F.A. Ponce, Growth of high-quality AlN layers on sapphire substrates at relatively low temperatures by metalorganic chemical vapor deposition, Phys. Status Solidi B 252 (2015) 1089–1095, https://doi.org/10.1002/pssb.201451571.

[14] L.S. Zhang, F.J. Xu, J.M. Wang, C.G. He, W.W. Guo, M.G. Wang, B.W. Sheng, L. Lu, Z.X. Qin, X.Q. Wang, B. Shen, High-quality AlN epitaxy on nano-patterned sapphire substrates prepared by nano-imprint lithography, Sci. Rep. 6 (2016) 35934.

[15] J.W. Ben, X.J. Sun, Y.P. Jia, K. Jiang, Z.M. Shi, H.N. Liu, Y. Wang, C.H. Kai, Y. Wu, D.B. Li, Defect evolution in AlN templates on PVD-AlN/sapphire substrates by thermal annealing, CrystEngComm 20 (2018) 4623, https://doi.org/10.1039/C8CE00770E.

[16] AlN substrate products. http://www.hexatechinc.com/aln-wafer-sales.html.

[17] H. Jeon, C. Lee, M. Yang, S.N. Yi, H.S. Ahn, Y.M. Yu, S.C. Lee, S.W. Kim, N. Sawaki, Thick AlN epilayer grown by using the HVPE method, J. Korean Phys. Soc. 67 (2015) 643–647.

[18] J. Neugebauer, C.G. Van Der Walles, Gallium vacancies and the yellow luminescence in GaN, Appl. Phys. Lett. 69 (1999) 503–505, https://doi.org/10.1063/1.117767.

[19] M. Julkarnain, N. Kamata, T. Fukuda, Y. Arakawa, Yellow luminescence band in undoped GaN revealed by two-wavelength excited photoluminescence, Opt. Mater. 60 (2016) 481–486, https://doi.org/10.1016/j.optmat.2016.09.003.

[20] A.R. Micheal, M. Hadis, Luminescence properties of defects in GaN, J. Appl. Phys. 97 (2005) 061301, https://doi.org/10.1063/1.1868059.

[21] Z.Q. Fang, D.C. Look, P. Visconti, D.F. Wang, C.Z. Lu, F. Yun, H. Morkoç, S.S. Park, K.Y. Lee, Deep centers in a free-standing GaN layer, Appl. Phys. Lett. 78 (2001) 2178–2180, https://doi.org/10.1063/1.1361273.

[22] K.B. Nam, M.L. Nakarmi, J.Y. Lin, H.X. Jiang, Deep impurity transitions involving cation vacancies and complexes in AlGaN alloys, Appl. Phys. Lett. 86 (2005) 222108, https://doi.org/10.1063/1.1943489.

[23] N. Nepal, M.L. Nakarmi, J.Y. Lin, H.X. Jiang, Photoluminescence studies of impurity transitions in AlGaN alloys, Appl. Phys. Lett. 89 (2006) 092107, https://doi.org/10.1063/1.2337856.

[24] R. Collazo, J.Q. Xie, E.G. Benjamin, Z. Bryan, R. Kirste, M. Hoffmann, R. Dalmau, B. Moody, Y. Kumagai, T. Nagashima, Y. Kubota, T. Kinoshita, A. Koukitu, D.L. Irving, Z. Sitar, On the origin of the 265 nm absorption band in AlN bulk crystals, Appl. Phys. Lett. 100 (2012) 191914, https://doi.org/10.1063/1.4717623.

[25] N. Nepal, K.-B. Nam, M.-L. Nakarmi, J.-Y. Lin, H.-X. Jiang, J.-M. Zavada, R.-G. Wilson, Optical properties of the nitrogen vacancy in AlN epilayers, Appl. Phys. Lett. 84 (2004) 1090, https://doi.org/10.1063/1.1648137.

[26] Q.M. Yan, J. Anderson, M. Scheffler, C.G. Van Der Walles, Origins of optical absorption and emission lines in AlN, Appl. Phys. Lett. 105 (2014) 111104, https://doi.org/10.1063/1.4895786.

[27] G. Namkoong, E. Trybus, K.K. Lee, M. Moseley, W.A. Doolittle, D.C. Look, Metal modulation epitaxy growth for extremely high hole concentrations above 10^{19} cm^3 in GaN, Appl. Phys. Lett. 93 (2008) 172112, https://doi.org/10.1063/1.3005640.

[28] P.B. Brendan, A.M.F. Chloe, J.M. Joseph, A.C. Evan, W.A. Doolittle, S. Wang, A.M. Fischer, F.A. Ponce, Comprehensive study of the electronic and optical behavior of highly degenerate p-type Mg-doped GaN and AlGaN, J. Appl. Phys. 117 (2015) 045710, https://doi.org/10.1063/1.4906464.

[29] T. Kinoshita, T. Obata, H. Yanagi, S. Inoue, High p-type conduction in high-Al content Mg-doped AlGaN, Appl. Phys. Lett. 102 (2013) 012105, https://doi.org/10.

1063/1.4773594.
[30] V. Kueller, A. Knauer, F. Brunner, A. Mogilatenko, I.M. Kneiss, M. Weyers, Investigation of inversion domain formation in AlN grown on sapphire by MOVPE, Phys. Status Solidi C 9 (2012) 496–498, https://doi.org/10.1002/pssc.201100495.
[31] S.J. Bak, D.H. Mun, K.C. Jung, J.H. Park, H.J. Bae, I.W. Lee, T.S. Oh, Effect of Al pre-deposition on AlN buffer layer and GaN film grown on Si (111) substrate by MOCVD, Electr. Mater. Lett. 9 (2013) 367–370.
[32] Q. Bao, J. Luo, C. Zhao, Mechanism of TMAl pre-seeding in AlN epitaxy on Si (111) substrate, Vacuum 101 (2014) 184–188, https://doi.org/10.1016/j.vacuum.2013.08.015.
[33] K.N. Tu, J.W. Maye, L.C. Feldman, Electronic Thin Film Science, Macmillan College Publishing Company Inc., London, 1992, pp. 225–230.
[34] A.F. Wright, Elastic properties of zinc-blende and wurtzite AlN, GaN, and InN, J. Appl. Phys. 82 (1997) 2833–2839, https://doi.org/10.1063/1.366114.
[35] W.Y. Han, Z.W. Zhang, Z.M. Li, Y.R. Chen, H. Song, G.Q. Miao, H. Jiang, High performance back-illuminated MIS structure AlGaN solar-blind ultraviolet photodiode, J. Mater. Sci.: Mater. Electron. 29 (2018) 9077–9082.
[36] T. Detchprohm, K. Hiramatsu, K. Itoh, I. Akasaki, Relaxation process of the thermal strain in the GaN/α-Al_2O_3 heterostructure and determination of the intrinsic lattice constants of GaN free from the strain, Jpn. J. Appl. Phys. 31 (1992) L1454, https://doi.org/10.1143/JJAP.31.L1454.
[37] A.R. Denton, N.W. Ashcroft, Vegard's law, Phys. Rev. A 43 (1991) 3161, https://doi.org/10.1103/PhysRevA.43.3161.
[38] M.J. Hou, Z.X. Qin, L.S. Zhang, T.Y. Han, M.X. Wang, F.J. Xu, X.Q. Wang, T.J. Yu, Z.Y. Fang, B. Shen, Excitonic localization at macrostep edges in AlGaN/AlGaN multiple quantum wells, Superlattices Microstruct. 104 (2017) 397–401, https://doi.org/10.1016/j.spmi.2017.02.051.
[39] I. Bryan, Z. Bryan, S. Mita, A. Rice, L. Hussey, C. Shelton, J. Tweedie, J.P. Maria, R. Collazo, Z. Sitar, The role of surface kinetics on composition and quality of AlGaN, J. Cryst. Growth 451 (2016) 65–71, https://doi.org/10.1016/j.jcrysgro.2016.06.055.
[40] K. Jiang, X.J. Sun, J.W. Ben, Z.M. Shi, Y.P. Jia, Y. Wu, C.H. Kai, Y. Wang, D.B. Li, Suppressing the compositional nonuniformity of AlGaN grown on HVPE-AlN template with large macro-steps, CrystEngComm 21 (2019) 4864–4873, https://doi.org/10.1039/C9CE00608G.
[41] H.S. Kim, R.A. Mair, J. Li, J.Y. Lin, H.X. Jiang, Time-resolved photoluminescence studies of $Al_xGa_{1-x}N$ alloys, Appl. Phys. Lett. 76 (2000) 1252–1254, https://doi.org/10.1063/1.126000.
[42] H. Sun, F. Wu, Y.J. Park, T.M. Al tahtamouni, K.-H. Li, N. Alfaraj, T. Detchprohm, R.D. Dupuis, X. Li, Influence of TMAl preflow on AlN epitaxy on sapphire, Appl. Phys. Lett. 110 (19) (2017) 192106, https://doi.org/10.1063/1.4983388.
[43] H.D. Sun, F. Wu, T.M. Al Tahtamouni, N. Alfaraj, K.H. Li, T. Detchprohm, R.D. Dupuis, X.H. Li, Structural properties, crystal quality and growth modes of MOCVD-grown AlN with TMAl pretreatment of sapphire substrate, J. Phys. D Appl. Phys. 50 (2017) 395101, https://doi.org/10.1088/1361-6463/aa8503.
[44] K. Jiang, X.J. Sun, J.W. Ben, Y.P. Jia, H.N. Liu, Y. Wang, Y. Wu, C.H. Kai, D.B. Li, The defect evolution in homoepitaxial AlN layers grown by high-temperature metal-organic chemical vapor deposition, CrystEngComm 20 (2018) 2720–2728, https://doi.org/10.1039/C8CE00287H.
[45] T. Onuma, S.F. Chichibu, A. Uedono, T. Sota, P. Cantu, T.M. Katona, J.F. Keading, S. Keller, U.K. Mishra, S. Nakamura, S.P. DenBaars, Radiative and nonradiative processes in strain-free $Al_xGa_{1-x}N$ films studied by time-resolved photoluminescence and positron annihilation techniques, J. Appl. Phys. 95 (2004) 2495–2504, https://doi.org/10.1063/1.1644041.
[46] S.F. Fan, Z.X. Qin, C.G. He, M.J. Hou, X.Q. Wang, B. Shen, W. Li, W.Y. Wang, D.F. Mao, P. Jin, J.C. Yan, P. Dong, Optical investigation of strong exciton localization in high Al composition $Al_xGa_{1-x}N$ alloys, Opt. Express 21 (2013) 24497–24503, https://doi.org/10.1364/OE.21.024497.
[47] H. Gotoh, H. Ando, T. Takagahara, H. Kamada, A. Chavez-Pirson, J. Temmyo, Effects of dimensionality on radiative recombination lifetime of excitons in thin quantum boxes of intermediate regime between zero and two Dimensions, Jpn. J. Appl. Phys. 36 (1997) 4204–4208, https://doi.org/10.1143/JJAP.36.4204.
[48] J.S. Huang, X. Dong, X.D. Luo, X.L. Liu, Z.Y. Xu, W.K. Ge, Localized exciton dynamics in AlInGaN alloy, Solid State Commun. 126 (2003) 473–477, https://doi.org/10.1016/S0038-1098(03)00207-2.